HHS Public Access

Author manuscript

Nat Photonics. Author manuscript; available in PMC 2016 June 09.

Published in final edited form as:

Nat Photonics. 2015 ; 9: 563–571. doi:10.1038/nphoton.2015.140.

Guidestar-assisted wavefront-shaping methods for focusing light into biological tissue

Roarke Horstmeyer[*], **Haowen Ruan**, and **Changhuei Yang**

Department of Electrical Engineering, California Institute of Technology, Pasadena, California 91125, USA

Abstract

In the field of biomedical optics, optical scattering has traditionally limited the range of imaging within tissue to a depth of one millimetre. A recently developed class of wavefront-shaping techniques now aims to overcome this limit and achieve diffraction-limited control of light beyond one centimetre. By manipulating the spatial profile of an optical field before it enters a scattering medium, it is possible to create a micrometre-scale focal spot deep within tissue. To successfully operate *in vivo*, these wavefront-shaping techniques typically require feedback from within the biological sample. This Review summarizes recently developed 'guidestar' mechanisms that provide feedback for intra-tissue focusing. Potential applications of guidestar-assisted focusing include optogenetic control over neurons, targeted photodynamic therapy and deep tissue imaging.

Most vertebrate organisms, including humans, are optically turbid. Our cellular structures generally exhibit a heterogeneous refractive index. A spatially varying refractive index causes light to scatter, which prevents us from seeing beneath the first few layers of biological material, or from focusing visible radiation deep within biological tissue.

Wavelengths outside the optical spectrum, which scatter less through organic material, are widely available for probing deeper within biological organisms. For example, X-rays offer excellent resolution in computed tomography, and magnetic resonance imaging remains an invaluable tool for medical diagnosis. However, these well-known techniques offer a limited ability to control and manipulate cells or molecules. In contrast, a large suite of recently developed optical methods can now both probe and activate biochemical content using visible light. Example applications include the photochemical activation of drugs[1], the photorelease of biomolecules[2], stimulation of neural activity through optogenetic tags[3] and imaging with fluorescent markers[4]. Similar insights may also help form images at unprecedented resolution[5]. However, optical scattering still restricts many of these advances to the outermost layers of tissue.

[*]Correspondence should be addressed to R.H., roarke@caltech.edu.

Author contributions

All authors contributed equally to this work.

Competing financial interests

The authors declare no competing financial interests.

When a beam of light enters skin, its photons bounce around so many times that after a certain distance (the transport mean free path (TMFP), l^*), they face an equal probability of moving in any direction. This diffusion of an incident beam of light into a general 'glow' happens quite quickly in most biological tissue, typically at a depth[6] of $l^* \approx 1$ mm. Until recently, most optical techniques for imaging deep within tissue would primarily utilize only unscattered (that is, ballistic) photons (for example, confocal imaging, two-photon microscopy[7] and optical coherence tomography[8]). Because the number of ballistic photons decays exponentially with depth, the TMFP has long persisted as a supposedly impassable barrier for diffraction-limited imaging[9].

Recently, researchers demonstrated that photons retain a significant amount of information after scattering many times through disordered material[10], such as biological tissue[11]. Instead of throwing these seemingly randomized photons away, a host of new technologies now capture and extract information from multiply scattered light. By measuring the spatial phase profile of an optical field exiting tissue, one can computationally recover an ideal wavefront shape that, when sent back into tissue, will focus to a micrometre-scale spot. This optimization process closely relates to the principle of time reversal, which suggests that a beam of light may be guided backwards through a disordered medium to effectively 'cancel' its scattering effects.

Actively correcting random optical wavefront distortions is a common practice in astronomy[12]. By measuring how the atmosphere perturbs light from a 'guidestar' (that is, an approximate point source of light), adaptive optics (AO) systems adjust and sharpen images within most ground-based telescopes. The 'wavefront-shaping' technologies covered by this Review share a common foundation with the principle of AO, but extend operation into the biophotonic setting, where heavy optical scattering dominates. Correspondingly, instead of removing low-order aberrations to image 'across' distortion clearly, wavefront shaping aims for a generally more useful goal in the field of biology: to send light 'into' tissue, thereby forming a tight focus within.

Recent work has adopted one of two guidestar-based strategies. In this Review, we classify these two strategies as using either a 'feedback' or 'conjugation' guidestar, and detail each in separate sections. Outside of the biological setting, an experimentalist can typically manipulate light on both sides of a scattering material, and thus does not usually need the assistance of a guidestar. Mosk *et al.* offer a thorough Review of wavefront shaping through non-biological disordered media[13]. This Review will focus on techniques that hold promise for controlling light inside *in vivo* tissue, where access is primarily limited to one side of the scattering material. Example guidestars for biological application include fluorescence markers[14,15], nonlinear optical particles[16], photo-acoustic feedback[17–20], ultrasound-enabled focusing[21–23] and kinematic targets[24,25]. Before discussing details about each wavefront-shaping strategy, we first present a simple mathematical model to explain how to account for optical scattering using a properly designed wavefront.

The propagation of light within tissue

First, it is helpful to break down the complex journey of a single photon through tissue into a discrete number of scattering events. Following this short discussion, we will replace our particle viewpoint with a wave model, which allows us to describe wavefront shaping more easily. We may characterize a homogeneous scattering medium by its scattering mean free path l, which specifies the average distance travelled by a photon between two scattering events. A typical value for l in tissue is 100 μm (ref. 6). When imaging tissue samples thicker than l, conventional microscopes will also capture scattered photons, which deteriorate image quality. Techniques like confocal and multiphoton excitation microscopy filter out scattered photons, thereby allowing imaging beyond one scattering mean free path.

Although these techniques have transformed biomedical imaging over several decades, confocal and multiphoton microscopes still face challenges when operating beneath the tissue TMFP depth, $l^* = l/(1 - g) \approx 1$ mm (refs 9,26). The distance l^* depends on both the mean free path l and an anisotropy parameter, $g \approx 0.8–0.98$, which takes into account the forward-scattering nature of tissue (Fig. 1a). The TMFP depth matches previously derived penetration upper limits for imaging methods that rely on ballistic photons[6,7,9]. Although several recent techniques have improved ballistic photon collection using spatial field correlations[27] or combined spatial and coherence gating[28], many elastically scattered photons remain significantly beyond one millimetre. As the effects of tissue absorption are minimal until centimetre-scale depths[29], an ideal technique would account for, as opposed to block, multiply scattered photons.

Accurate models of highly scattered light in this deep, diffusive regime exist. Diffuse optical tomography[30,31] and fluorescence molecular tomography[32] can computationally reconstruct limited-resolution images of macroscopic structure well beyond several TMFP. However, their resolution deteriorates with imaging depth[6]. Furthermore, such techniques do not take into account the effects of interference, which is the hallmark of coherent light. As we will see, correlations within a complex optical field preserve a relationship between all possible paths that light can follow while scattering. By mapping out the relative optical phase difference between each path, it is possible to control coherent light, deep within tissue, at the diffraction limit.

It is now convenient to treat light as a wave, which, for simplicity, we assume is coherent. A monochromatic optical wave field, $u(\mathbf{r})$, propagates through a linear scattering material with a variable index of refraction, $n(\mathbf{r})$, following the scalar wave equation $\nabla^2 u(\mathbf{r}) + k^2 n^2(\mathbf{r})\, u(\mathbf{r}) = 0$. Here, $k = 2\pi/\lambda$ denotes the wavevector and λ is the optical wavelength. Often, one has discrete control over N spatial degrees of freedom of an optical ‘input’ field, u_a, before it enters a scattering sample, typically using a spatial light modulator (SLM, Fig. 1). In this scenario, it is useful to define the input field as a row vector $\mathbf{u}_a$ that contains N complex entries. A limited numerical aperture, or the diffraction limit, allows unambiguous discretization of u_a into a vector using the Nyquist–Shannon sampling theorem.

We now consider an arbitrary ‘target’ plane of interest at a depth L within a scattering sample (Fig. 2a), where we hope to focus light. We may spatially discretize this target plane

into M entries with a spacing of $\lambda/2n$. In many wavefront-shaping experiments, this plane is external to the scatterer and contains an M-pixel detector. Although in practice both input and target fields typically exist along two spatial dimensions, for simplicity we will primarily consider each field along one dimension. Once discretized, the forward-propagating input field vector $\mathbf{u}_a$ now connects to the optical field at the target plane $\mathbf{u}_b$ through the matrix equation $\mathbf{u}_a\mathbf{T} = \mathbf{u}_b$. Here, we define scattering between the input and target planes, caused by an inhomogeneous refractive index in the wave equation, using a transformation matrix $\mathbf{T}$ with $N \times M$ complex entries. If light at our embedded target plane is primarily forward-travelling, as in the case of highly anisotropic scattering, then $\mathbf{T}$ is the well-known transmission matrix[33]. Deep within tissue, where scattering becomes isotropic, the total target field includes contributions from all scatterer regions. However, a linear relationship will still connect the total field at both planes. Although not included here for simplicity, any reflected light may also be modelled within the $2N \times 2M$ 'scattering' matrix[34,35]. Finally, for graphical clarity we adopt the convention of multiplying $\mathbf{T}$ from the left, with a row vector, to denote light propagating into tissue (Fig. 2a). We will use column vectors to denote light propagation in the opposite direction (Fig. 2b).

If a point source sequentially shifts across the input plane, then scattering will cause the target optical field to fluctuate. We mathematically express an input field containing a point source in its ith discrete location as $\mathbf{u}_a = \boldsymbol{\delta}_i$, where we define $\boldsymbol{\delta}_i$ as the ith unit vector. For any discrete input location x_a, this particular input field satisfies $\mathbf{u}_a[x_a = i] = 1$ and $\mathbf{u}_a[x_a \neq i] = 0$. The ith resulting target field is the matrix product $\boldsymbol{\delta}_i\mathbf{T} = \mathbf{t}_i$, where $\mathbf{t}_i$ denotes the ith transmission matrix row. Scattering almost always results in a random field with a grainy appearance, called speckle. If the medium is sufficiently thick and turbid, then the embedded speckle field's spatial variations approach a correlation distance of $\lambda/2n$ (that is, the speckle becomes 'fully developed'[36]). In this limit, each discrete element of $\mathbf{t}_i$ approaches a complex random variable with a circularly symmetric Gaussian distribution, which is not correlated with its neighbours. If the medium is also thick enough to satisfy $L \gg l$, then light is in the multiple-scattering regime[37]. Here, a small change in the input wavefront (for example, a shift to input unit vector $\boldsymbol{\delta}_{i+1}$) will produce a nearly uncorrelated, yet still fully developed, target speckle field. At such depths, it thus becomes fair to approximate each element of the transmission matrix as an uncorrelated random variable.

Remaining sources of correlation within $\mathbf{T}$, caused for example by energy conservation and a finite thickness, are of both practical application and ongoing theoretical interest[38]. One form of correlation, termed the 'memory effect'[37], helps computational imaging techniques recover objects hidden behind thin, scattering layers[39,40] such as tissue[41]. However, these methods require a finite separation between scatterer and object, and thus cannot directly focus or image to a plane embedded within tissue. The high anisotropy of tissue offers a second useful form of correlation that allows scanning across an embedded plane over a limited range[42].

Wavefront shaping using feedback guidestars

The transmission matrix model informs us of the amplitude and phase of light at an embedded target plane, given an arbitrary input field. If the complex matrix $\mathbf{T}$ is known, then

we can also invert a scattering system to create any desired target field using a specifically designed input field (for example, to focus within tissue). We may express this input field solution mathematically by computing a matrix inverse, $\mathbf{u}_a = \mathbf{u}_b\mathbf{T}^{-1}$ (or a pseudo-inverse for rectangular $\mathbf{T}$). If $\mathbf{T}$ is unitary, then we can equivalently apply a conjugate transpose, $\mathbf{u}_a = \mathbf{u}_b\mathbf{T}^*$. Although this is typically not an equivalent operation, conjugation closely approximates inversion when the scattering and detection system has minimal loss[43]. In practice, combining both matrix inversion and conjugation into one operator helps overcome experimental noise[44]. Given an SLM to define the input field, we may apply the following three steps to overcome optical scattering. First, scan through N different orthogonal input fields on the SLM and measure each resulting complex target field. For example, if each input field is the ith unit vector δ_i, then each target field is the ith matrix row $\mathbf{t}_i$. Interferometry is typically required to measure the complex target field. Next, construct the transmission matrix $\mathbf{T}$ from the N measured target fields (that is, place each $\mathbf{t}_i$ into the ith row of $\mathbf{T}$). Finally, solve the above inverse matrix equation to create any desired target field $\mathbf{u}_b$, by wavefront shaping with the SLM.

Transmission matrix measurement and inversion can deliver arbitrary images through disordered materials[33,44–46]. It is also possible to measure the scattering response of reflected light in a similar fashion[47]. Although this is an elegant way to overcome optical scattering, measuring each target speckle field $\mathbf{t}_i$ from within tissue is practically challenging. One experimental technique uses the photo-acoustic effect[17] (Fig. 3a). Here, light at an embedded plane induces an ultrasound signal through localized thermal expansion[48]. This time-varying ultrasound response, detected with an external transducer, offers an indirect estimate of local light intensity along one scatterer dimension. Linearly translating the detector system, while scanning through SLM patterns at each unique location, builds up a full transmission matrix (Fig. 3b). If the experimental goal is to form a single focus, however, it is not necessary to measure the entire transmission matrix.

If we are just concerned with the value of the target field $\mathbf{u}_b[c]$ at one fixed target location $x_b = c$ within tissue, we do not need to multiply our input field with the entire transmission matrix. Instead, we must only consider the cth column of the transmission matrix and compute an inner product. We use a bar to distinguish this cth column as the column vector $\bar{\mathbf{t}}_c$. We may determine the scalar target field formed at location c by any input field vector $\mathbf{u}_a$ with the inner product, $\mathbf{u}_a\bar{\mathbf{t}}_c = \mathbf{u}_b[c]$ (Fig. 3c). Here, we see that only the N values within $\bar{\mathbf{t}}_c$ are needed to map fully the scattering relationship between the input plane and the field at the cth embedded target location. Just like measuring and conjugating the transmission matrix to undo scattering across the entire target plane, measuring and computing the conjugate transpose of $\bar{\mathbf{t}}_c$ enables focusing at the target point $x_b = c$. This is clear if we set $\mathbf{u}_a = \bar{\mathbf{t}}_c^*$ in the above inner product, such that $\bar{\mathbf{t}}_c^*\bar{\mathbf{t}}_c \approx 1$, which is the maximum possible normalized amplitude at target location c.

Matching our procedure to measure $\mathbf{T}$, one may determine $\bar{\mathbf{t}}_c$ by scanning through orthogonal SLM patterns[10,49]. Now, however, only a single pixel detector records the target field. Or, instead of cycling through orthogonal SLM patterns, feedback between the single detector and the SLM (for example, with a genetic or hill-climbing algorithm) encourages

speedy maximization of delivered light intensity[35,50]. With either approach, the ideal SLM-shaped input field remains the conjugated transmission matrix column vector[51] $\bar{\mathbf{t}}_c^*$, and the focal spot brightness increases linearly with the number of conjugated optical modes[10].

For most biological experiments, it is not possible to embed a physical detector (for example, a photodiode) into tissue to measure $\bar{\mathbf{t}}_c$. Similar to indirectly measuring the transmission matrix, one may instead use a signal that is correlated with localized light intensity to provide SLM feedback[52]. We refer to this mechanism as a 'feedback guidestar', of which there are several varieties (Fig. 3c–e). One of the first demonstrations of overcoming scattering with a feedback guidestar used a fluorescent bead embedded within a disordered material. A feedback algorithm that connected the fluorescence intensity (detected outside the material) to an input-shaping SLM experimentally enhanced the fluorescent excitation by a factor of 20 or more[14,53].

A fluorescent guidestar often requires invasive positioning and fixes light delivery to a single location. A moveable ultrasound focal spot, which frequency-shifts light[54] through refractive index modulation and scatterer displacement, offers a non-invasive feedback alternative[55]. Because ultrasound scatters weakly in tissue, it provides a useful mechanism for extracting optical information from an embedded target plane. Alternatively, instead of sending in ultrasound and detecting modulated light, an externally measured photo-acoustic signal also indicates the local strength of internal light, as mentioned earlier. Standard photo-acoustic 'guidestar' feedback originates from a single spot, and is limited to the acoustic resolution[18,19]. Nonlinear photo-acoustic feedback[20] helps to focus near the optical resolution limit (5–7 μm, Fig. 3d), although not yet within thick biological tissue.

It is also possible to create guidestar-like feedback by monitoring the two-photon fluorescence signal generated directly inside a scattering sample[56,57] (Fig. 3e). Or, one may track the coherent interference of backscattered light from different sample layers[58,59]. These two examples achieve feedback with optical mechanisms that are also shared by other biomedical imaging modalities: two-photon excitation microscopy and optical coherence tomography (OCT), respectively. Next, we briefly detail how AO techniques, which are also used to improve two-photon excitation imaging and OCT performance, apply to wavefront shaping with feedback guidestars.

As explained previously, AO is the imaging complement of wavefront shaping: the former passively removes aberrations after light has propagated from an object of interest, whereas the latter actively shapes light so that it can pass through an aberrative medium (for example, to form a focus). In early applications, AO applied similar feedback algorithms to measure and correct image distortions caused by the atmosphere[12] or the eye's lens[60]. Later, AO microscopes applied fluorescence feedback to remove low-order aberrations from ballistic light[61]. As with wavefront shaping, AO does not necessarily require a specific physical feedback guidestar. Systems may also apply feedback from two-photon[62] or fluorescent[63] image intensities. In addition to removing image aberrations, AO microscopes also commonly correct for distortions within their illumination path[64]. This closely matches the goal of wavefront shaping. Furthermore, recent AO microscopes now also correct for complex image distortions caused by non-ballistic light[57,65–67].

Although conceptually similar, three key differences help distinguish guidestar-based wavefront shaping from AO techniques. First, many AO set-ups focus light into a guidestar from the input side (for example, laser guidestars in astronomy and ophthalmology). Significant scattering precludes the ability to focus light directly into a guidestar within tissue. This gives rise to our list of inventive feedback mechanisms (Table 1). Second, a wavefront correction map in AO can remove aberrations over a finite area known as the isoplanatic patch[68]. The isoplanatic patch beneath 1 TMFP in tissue is limited to several square micrometres or less. This limits the relevance of one optimal input wavefront to a specific target location. Finally, the number of parameters (and hence measurements) required to fit an AO aberration map is typically small. An AO transmission matrix contains of the order of $N \approx 10^2$ modes. In contrast, deep-tissue guidestars require many more measurements to map accurately the $N \approx 10^5$ or more independent optical modes in the diffusive regime[13].

Time reversal and phase conjugation

Feedback guidestar techniques measure the scattering response of tissue sequentially over time. Unfortunately, accurate focusing can require millions of unique measurements, and the scattering response of *in vivo* tissue changes on a sub-second timescale[69,70]. To overcome this time constraint, a helpful strategy would involve measuring the scattering response of tissue in a parallel manner. By adopting the principle of time reversal, or 'optical phase conjugation' (OPC), it is possible to refocus light to a guidestar spot from a single snapshot.

To outline the principle of OPC, let us assume that an ideal guidestar emits a monochromatic optical wave with frequency ω. At any position **r** and time t within the scatterer, we may express this emitted scalar field as $u(\mathbf{r}, t) = \mathrm{Re}\{A(\mathbf{r}) \exp[i(\phi(\mathbf{r}) - \omega t)]\}$. Here, A specifies the field amplitude and ϕ defines its spatially varying phase. Given propagation within a lossless medium, the wave equation remains time-invariant. For any forward-propagating field $u(\mathbf{r}, t)$ that is scattering out of the medium, there also exists a wavefunction $u' = u(\mathbf{r}, -t)$ that will precisely retrace the path of u back through every scattering interaction to its original guidestar location. If the constant phase lines for u must satisfy $\phi(\mathbf{r}) = \omega t$, then the constant phase lines of u' must satisfy $\phi(\mathbf{r}) = -\omega t$. It is clear the phase lines of u' also satisfy the relation $-\phi(\mathbf{r}) = \omega t$.The left-hand side of this equation represents the spatial phase conjugate of u. We can therefore 'time reverse' an arbitrary field u back into its original guidestar spot by conjugating its spatial phase, and then allowing it to continue travelling ahead in time.

To describe OPC within our linear algebra framework, we represent the light emerging from the target plane's guidestar as $\bar{\mathbf{u}}_b$, where the bar denotes a column vector. We assume time-reversal symmetry to express its transformation to the input plane as $\bar{\mathbf{u}}_a = \mathbf{T}\bar{\mathbf{u}}_b$. Light propagating from the target to input plane, as a column vector, now multiplies into our transmission matrix from the right (Fig. 2b,d). In practice, sample absorption and a limited detection aperture prevent collection of the complete guidestar field[35]. Despite this challenge, the following phase-conjugation strategy can still be used to focus light into tissue. First, create a discrete point source of light at a specific location $x_b = c$ within tissue: $\bar{\mathbf{u}}_b = \bar{\delta}_c$, the cth unit column vector. Next, capture the resulting scattered field at the input plane: $\bar{\mathbf{u}}_a = \mathbf{T}\bar{\delta}_c = \bar{\mathbf{t}}_c$, the cth column of **T** (Fig. 4a). Finally, phase-conjugate the detected

field into $\bar{\mathbf{t}}_c^*$ and send the conjugate-transposed field back towards the target plane: $\bar{\mathbf{t}}_c^*\mathbf{T}=\boldsymbol{\delta}_c+\boldsymbol{\varepsilon}$. This conjugated field re-focuses to a discrete spot at the guidestar origin (Fig. 4b). Incomplete measurement and imperfect conjugation of $\bar{\mathbf{t}}_c$ also typically introduces a finite background field $\boldsymbol{\varepsilon}$. Note this expression closely matches the final result of our previous 'feedback guidestar' strategy. Here, OPC directly measures and conjugates the vector $\bar{\mathbf{t}}_c$, whereas feedback from the target plane determines the elements of $\bar{\mathbf{t}}_c^*$ in sequence.

Several experimental techniques are available to implement OPC. Early work used a deformable mirror to display the conjugate map of distorted light from a guidestar, which corrected for atmospheric turbulence[12]. Typical deformable mirrors can only reshape a small number of low-order optical modes. Similarly early experiments also tested holograms for conjugating light through fixed distortions[71,72]. Unlike a deformable mirror, holograms can record and modify millions of wavefront modes. Nonlinear optical phenomena may also act like a 'conjugate mirror'[73] to conjugate light through dynamic distortions[74]. Examples include stimulated Brillouin scattering, multiple-wave mixing and the photorefractive effect[75,76]. Although these approaches offer quick response times, the analog nature of nonlinear techniques precludes the ability to adjust their conjugation maps computationally.

The first OPC experiment to focus light through thick biological tissue involved using a hologram to record and conjugate the scattered field[11]. Shortly thereafter, focusing through tissue was achieved with digital optical phase conjugation (DOPC), which interferometrically measures an optical field on a digital detector, and then creates its phase conjugate using a pixel-to-pixel matched SLM[77]. A similar strategy can compensate for and combine multiple beams within an optical fibre[78]. Here, unlike early phase-conjugation work with deformable mirrors, DOPC uses a modern SLM that contains several million individually addressable elements. Thus, DOPC may compensate for complex optical transformations that involve millions of propagation modes, such as diffusive scattering in tissue[13]. Furthermore, unlike analog holograms, DOPC can digitally correct for minor setup misalignments[79] and can in principle shape either continuous or pulsed beams of arbitrary power.

Wavefront shaping with conjugation guidestars

With direct access to the target plane, OPC can measure and conjugate arbitrary fields through *ex vivo* tissue[11]. Without access, for instance during an *in vivo* experiment, OPC requires an effective 'conjugation guidestar'that can emit light for subsequent refocusing. Fluorescent excitation within the retina is one of the first conjugation guidestars applied in a biological context[80]. Here, a focused beam stimulates a small incoherent light source at the retina, which is externally measured to compensate for aberrations. Embedded fluorescent microspheres[81] and proteins[82,83] serve as similar conjugation beacons in AO microscopy. It is also possible to implement conjugation-based correction using coherence gating[84] or OCT[85]. Here, we review recent extensions of this early conjugation work into the regime of wavefront shaping, where wavefront distortions arise from deep within tissue. We summarize our list of conjugation guidestars in Table 1.

The first guidestar for conjugation-based focusing through turbid media used the nonlinear second-harmonic generation signal from a nanoparticle[16]. Shortly thereafter, Vellekoop *et al.* conjugated light from a fluorescent marker embedded beneath 0.5 mm of tissue[15] (Fig. 4c). Although the conjugated spot sizes of these techniques may approach the diffraction limit, both nonlinear and fluorescent guidestar signals originate from a fixed, spatially confined spot. Furthermore, their emission signals tend to be weak, and thus require long exposure times (≥1 s).

Focused ultrasound offers a conjugation guidestar that may be easily moved to different positions (Fig. 4d). As discussed in the context of feedback guidestars, a confined ultrasound focus can frequency-shift light at a defined spot within *in vivo* tissue[86]. Several experiments detected and phase-conjugated the ultrasound-modulated wavefront scattered from this finite spot (also termed a 'virtual source')[21–23]. The resolution of early time-reversed ultrasonically encoded (TRUE) demonstrations was fixed by the size of the ultrasound focus (25–50 μm). Although increasing the ultrasound frequency shrinks this spot size, it also decreases the number of photons modulated from deep within the tissue, thus presenting a trade-off between resolution and depth[87]. A potential solution to this resolution trade-off is iterative TRUE[88–90], whereby a feedback loop between the conjugated and detected fields can experimentally shrink the focus spot size by a factor of three (Fig. 4d).

Instead of improving TRUE focusing resolution with iterative feedback, one may also adopt a statistical approach known as the time reversal of variance-encoded light (TROVE)[91]. Conceptually, the relatively large TRUE focus modulates many optical speckles. The modulated field emerging from the tissue is thus a superposition of weighted optical fields, each originating from a unique location within the ultrasound spot. Standard TRUE simply detects and conjugates this entire superposition. Alternatively, through a series of measurements and application of Gaussian statistics, TROVE computationally decomposes this superposition back into its individually weighted components. By conjugating the appropriate component, it is possible to refocus to a single optical mode (that is, a focal spot one speckle wide, Fig. 4d, bottom). In combination with recent methods to perform TRUE over timescales of <10 ms (ref. 92), TROVE concepts may help establish a translatable, optical diffraction-limited guidestar for *in vivo* use.

Even without ultrasonic frequency encoding, multiple measurements of a time-varying optical field can still lead to a sharp, phase-conjugated focus within tissue. Two recent works (TRAP[24] and TRACK[25]) demonstrate this concept using a kinematic target embedded within a scattering material. First, a scattered field is measured when the target is absent from a volume of interest (u_0 in Fig. 4e). Second, a different scattered field is measured after the target has moved into the volume (u_1). Subtracting the first field from the second and conjugating the result will focus to the target location ($[u_1 - u_0]^*$ in Fig. 4e). An immediate application of the TRAP/TRACK principle is for *in vivo* flow cytometry. From two measurements of one 'guidestar' cell in motion, one may conjugate light to a tight focal spot. It is then possible to monitor the passage of any subsequent cells, for example, within the vein of interest, via external detection (Fig. 4e, bottom). Acquiring a sequence of speckle measurements may also help compute an image of such an embedded moving object, as recently considered in ref. [93].

Experimental development

Before achieving widespread biological application, guidestar techniques must first address tissue motion (Fig. 5). Any unknown change in scattering response between guidestar signal measurement and wavefront playback is a source of error. Macroscopic effects, like heartbeat and blood flow, are the primary cause of tissue movement. Even with an ideal playback wavefront, a sharp focus will quickly spread into random speckle during *in vivo* conjugation[69]. Studies indicate a system response time of less than 50 ms is needed to overcome movements in unconstrained tissue, or several seconds when the tissue is immobilized (that is, pinched)[69,70].

A select number of current setups, using either digital feedback[49] or nonlinear optical conjugation[92], operate within a 50 ms time window. An integrated detector and SLM[94], along with feedback algorithms that account for the temporal dynamics of the scattering medium[95,96], may lead to system response times below 1 ms. If the tissue sample can fit within an optical cavity, all-optical feedback can execute wavefront shaping at extremely fast, sub-microsecond timescales[97].

In parallel with increased speed, future wavefront-shaping technologies hope to push their focusing depth below one centimetre (that is, into the macroscopic regime[6]). At such depths, optical absorption becomes a limiting factor. Fluorescent and nonlinear guidestars with improved efficiencies will help overcome signal-to-noise ratio challenges. Models predict that ultrasound guidestars, which become attenuated at large depths, may currently extend to centimetre depth scales[87,98].

The computational nature of most recent wavefront-shaping work is one of its strongest assets. Mirroring the field of computational imaging, co-designed measurement and post-processing strategies can overcome experimental challenges. Examples include quick transmission matrix measurement without a reference beam[99], overcoming large amounts of experimental noise[50,100], shrinking the OPC focus width[91], and the related notion of a ‘computational’ guidestar, created through a combination of multiple measured fields exiting the tissue (for example, TRAP/TRACK).

Finally, most of the guidestar techniques reviewed here achieve refocusing with monochromatic light. The spectral dependence of optical scattering introduces additional degrees of freedom for wavefront control[101,102]. The related ability to temporally recompress an optical pulse using time reversal, as already well-studied with ultrasound[103], may also greatly enhance focused energy confinement. Although several recent electromagnetic implementations show promising benefits for spectral/temporal control[104–108], few achieve this control from just one side of the scattering material, which most biological settings require.

Biological applications

A variety of applications await both feedback and conjugation guidestar focusing in tissue. Many of these applications fall into one of two categories: energy delivery and information extraction. A well-established example from the former category is photodynamic therapy,

whose goal is to illuminate a diseased body region that contains a pre-administered photosensitizing drug. Applications include treatment of dermatological and ophthalmic disease, as well as solid tumors[1]. Highly concentrated optical power can also directly ablate tissue[109] or power implanted devices[110]. Photodynamic therapy, tissue ablation and power delivery currently suffer from limited optical control at directly accessible tissue regions (that is, less than one TMFP from the surface). A guidestar-based focus offers micrometre-scale optical control that can extend down multiple TMFP into the body, thereby possibly enabling new treatments.

Delivering energy to specific neurons within the brain can also help uncover how they communicate. When illuminated with sufficient light, optogenetic markers may activate or deactivate various physiological processes[3]. However, precise control over which neurons are optically activated is highly desired — inefficiencies and residual heating are a current limitation[111]. Initial demonstrations suggest that guidestar-based focusing may improve both the resolution and penetration depth of current optogenetic excitation techniques[67,112,113]. Furthermore, it may also assist with the joint goal of localizing fluorescence emitted from active neurons, potentially with subwavelength precision[114]. Although DOPC currently images arbitrary fluorescent structure at limited resolution[23], the above list of alternative goals will likely precede any significant improvement to its imaging performance. Finally, apart from exciting and detecting functionalized cells, shaped wavefronts can also manipulate particles within a scattering material[66,115]. Such optical manipulation within thick tissue may offer new tools for the active control of cellular and subcellular functions. In summary, guidestar-based methods can now successfully overcome turbidity to focus light deep within tissue. We will see many exciting biological applications over the next several years, which will likely grow in both number and impact as their technological foundation continues to develop.

Acknowledgments

We thank M. Jang, E. Zhou, B. Judkewitz, I. M. Vellekoop, J. Brake, H. Deng and M. Harfouche for helpful feedback during manuscript preparation. This work is supported by the National Institutes of Health (1DP2OD007307-01), the National Institutes of Health BRAIN Initiative (1U01NS090577-01) and a GIST-Caltech Collaborative Research Proposal (CG2012).

References

1. Huang Z. A review of progress in clinical photodynamic therapy. Technol. Cancer Res. T. 2005; 4:283–293.
2. Ellis-Davies GCR. Caged compounds: photorelease technology for control of cellular chemistry and physiology. Nature Methods. 2007; 4:619–628. [PubMed: 17664946]
3. Zhang F, et al. Optogenetic interrogation of neural circuits: technology for probing mammalian brain structures. Nature Protoc. 2010; 5:439–456. [PubMed: 20203662]
4. Lichtman JW, Conchello JA. Fluorescence microscopy. Nature Methods. 2005; 2:910–919. [PubMed: 16299476]
5. Thompson MA, Lew MD, Moerner WE. Extending microscopic resolution with single-molecule imaging and active control. Annu. Rev. Biophys. 2012; 41:321–342. [PubMed: 22577822]
6. Ntziachristos V. Going deeper than microscopy: the optical imaging frontier in biology. Nature Methods. 2010; 7:603–611. [PubMed: 20676081]

7. Helmchen F, Denk W. Deep tissue two-photon microscopy. Nature Methods. 2005; 2:932–940. [PubMed: 16299478]
8. Huang D, et al. Optical coherence tomography. Science. 1991; 254:1178–1181. [PubMed: 1957169]
9. Theer P, Denk W. On the fundamental imaging-depth limit in two-photon microscopy. J. Opt. Soc. Am. A. 2006; 23:3139–3149.
10. Vellekoop IM, Mosk AP. Focusing coherent light through opaque strongly scattering media. Opt. Lett. 2007; 32:2309–2311. [PubMed: 17700768]
11. Yaqoob Z, Psaltis D, Feld MS, Yang C. Optical phase conjugation for turbidity suppression in biological samples. Nature Photon. 2008; 2:110–115.
12. Hardy, JW. Adaptive Optics for Astronomical Telescopes. Oxford Univ. Press; 1998.
13. Mosk AP, Lagendijk A, Lerosey G, Fink M. Controlling waves in space and time for imaging and focusing in complex media. Nature Photon. 2012; 6:283–292.
14. Vellekoop IM, van Putten EG, Lagendijk A, Mosk AP. Demixing light paths inside disordered metamaterials. Opt. Express. 2008; 16:67–80. [PubMed: 18521133]
15. Vellekoop IM, Cui M, Yang C. Digital optical phase conjugation of fluorescence in turbid tissue. Appl. Phys. Lett. 2012; 101:081108.
16. Hsieh CL, Pu Y, Grange R, Psaltis D. Digital phase conjugation of second harmonic radiation emitted by nanoparticles in turbid media. Opt. Express. 2010; 18:12283–12290. [PubMed: 20588353]
17. Chaigne T, et al. Controlling light in scattering media non-invasively using the photoacoustic transmission matrix. Nature Photon. 2014; 8:58–64.
18. Kong F, et al. Photoacoustic-guided convergence of light through optically diffusive media. Opt. Lett. 2011; 36:2053–2055. [PubMed: 21633446]
19. Caravaca-Aguirre AM, et al. High contrast three-dimensional photoacoustic imaging through scattering media by localized optical fluence enhancement. Opt. Express. 2013; 21:26671–26676. [PubMed: 24216888]
20. Lai P, Wang L, Tay JW, Wang LV. Photoacoustically guided wavefront shaping for enhanced optical focusing in scattering media. Nature Photon. 2015; 9:126–132.
21. Xu X, Liu H, Wang LV. Time-reversed ultrasonically encoded optical focusing into scattering media. Nature Photon. 2011; 5:154–157.
22. Si K, Fiolka R, Cui M. Fluorescence imaging beyond the ballistic regime by ultrasound-pulse-guided digital phase conjugation. Nature Photon. 2012; 6:657–661.
23. Wang YM, Judkewitz B, Dimarzio CA, Yang C. Deep-tissue focal fluorescence imaging with digitally time-reversed ultrasound-encoded light. Nature Commun. 2012; 3:928. [PubMed: 22735456]
24. Ma C, Xu X, Liu Y, Wang LV. Time-reversed adapted-perturbation (TRAP) optical focusing onto dynamic objects inside scattering media. Nature Photon. 2014; 8:931–936.
25. Zhou EH, Ruan H, Yang C, Judkewitz B. Focusing on moving targets through scattering samples. Optica. 2014; 1:227–232. [PubMed: 25621302]
26. Horton NG, et al. In vivo three-photon microscopy of subcortical structures within an intact mouse brain. Nature Photon. 2013; 7:205–209.
27. Kang S, et al. Imaging deep within a scattering medium using collective accumulation of single-scattered waves. Nature Photon. 2015; 9:253–258.
28. Matthews TE, et al. Deep tissue imaging using spectroscopic analysis of multiply scattered light. Optica. 2014; 1:105–111.
29. Weissleder R, Ntziachristos V. Shedding light onto live molecular targets. Nature Med. 2003; 9:123–128. [PubMed: 12514725]
30. den Outer PN, Lagendijk A, Nieuwenhuizen TM. Location of objects in multiple-scattering media. J. Opt. Soc. Am. A. 1993; 10:1209–1218.
31. Arridge SR. Optical tomography in medical imaging. Inverse Probl. 1999; 15:R41–R93.
32. Ntziachristos V, Tung CH, Bremer C, Weissleder R. Fluorescence molecular tomography resolves protease activity in vivo. Nature Med. 2002; 8:757–760. [PubMed: 12091907]

33. Popoff SM, et al. Measuring the transmission matrix in optics: an approach to the study and control of light propagation in disordered media. Phys. Rev. Lett. 2010; 104:100601. [PubMed: 20366410]
34. Beenakker CWJ. Random-matrix theory of quantum transport. Rev. Mod. Phys. 1997; 69:731–808.
35. Vellekoop, IM. PhD thesis. Univ. Twente; 2008. Controlling the propagation of light in disordered scattering media.
36. Goodman, JW. Speckle Phenomena in Optics: Theory and Applications. Roberts and Co; 2007.
37. Feng S, Kane C, Lee PA, Stone AD. Correlations and fluctuations of coherent wave transmission through disordered media. Phys. Rev. Lett. 1988; 61:834–837. [PubMed: 10039442]
38. Wiersma DS. Disordered photonics. Nature Photon. 2013; 7:188–196.
39. Bertolotti J, et al. Non-invasive imaging through opaque scattering layers. Nature. 2012; 491:232–234. [PubMed: 23135468]
40. Katz O, Heidmann P, Fink M, Gigan S. Non-invasive single-shot imaging through scattering layers and around corners via speckle correlations. Nature Photon. 2014; 8:784–790.
41. Yang X, Pu Y, Psaltis D. Imaging blood cells through scattering biological tissue using speckle scanning microscopy. Opt. Express. 2014; 22:3405–3413. [PubMed: 24663630]
42. Judkewitz B, Horstmeyer R, Vellekoop IM, Papadopoulos IN, Yang C. Translation correlations in anisotropically scattering media. Nature Phys. 2015; 11:684–689.
43. Tanter M, Thomas JL, Fink M. Time reversal and the inverse filter. J. Acoust. Soc. Am. 2000; 108:223–234. [PubMed: 10923887]
44. Popoff S, Lerosey G, Fink M, Boccara AC, Gigan S. Image transmission through an opaque material. Nature Commun. 2010; 1:81. [PubMed: 20865799]
45. Kim M, et al. Maximal energy transport through disordered media with the implementation of transmission eigenchannels. Nature Photon. 2012; 6:581–585.
46. Cizmar T, Dholakia K. Exploiting multimode waveguides for pure fibre-based imaging. Nature Commun. 2012; 3:1027. [PubMed: 22929784]
47. Choi Y, et al. Measurement of the time-resolved reflection matrix for enhancing light energy delivery into a scattering medium. Phys. Rev. Lett. 2013; 111:243901. [PubMed: 24483661]
48. Wang LV, Hu S. Photoacoustic tomography: in vivo imaging from organelles to organs. Science. 2012; 335:1458–1462. [PubMed: 22442475]
49. Conkey DB, Caravaca-Aguirre AM, Piestun R. High-speed scattering medium characterization with application to focusing light through turbid media. Opt. Express. 2012; 20:1733–1740. [PubMed: 22274516]
50. Conkey DB, Brown AN, Caravaca-Aguirre AM, Piestun R. Genetic algorithm optimization for focusing through turbid media in noisy environments. Opt. Express. 2012; 20:4840–4849. [PubMed: 22418290]
51. Vellekoop IM, Mosk AP. Universal optimal transmission of light through disordered materials. Phys. Rev. Lett. 2008; 101:120601. [PubMed: 18851352]
52. Vellekoop IM. Feedback-based wavefront shaping. Opt. Express. 2015; 23:12189–12206. [PubMed: 25969306]
53. Vellekoop IM, Aegerter CM. Scattered light fluorescence microscopy: imaging through turbid layers. Opt. Lett. 2010; 35:1245–1247. [PubMed: 20410981]
54. Leutz W, Maret G. Ultrasonic modulation of multiply scattered light. Physica B. 1995; 204:14–19.
55. Tay JW, Lai P, Suzuki Y, Wang LV. Ultrasonically encoded wavefront shaping for focusing into random media. Sci. Rep. 2014; 4:3918. [PubMed: 24472822]
56. Katz O, Small E, Guan Y, Silberberg Y. Noninvasive nonlinear focusing and imaging through strongly scattering turbid layers. Optica. 2014; 1:170–174.
57. Tang J, Germain RN, Cui M. Superpenetration optical microscopy by iterative multiphoton adaptive compensation technique. Proc. Natl Acad. Sci. USA. 2012; 109:8434–8439. [PubMed: 22586078]
58. Fiolka R, Si K, Cui M. Complex wavefront corrections for deep tissue focusing using low coherence backscattered light. Opt. Express. 2012; 20:16532–16543.
59. Jang J, et al. Complex wavefront shaping for optimal depth-selective focusing in optical coherence tomography. Opt. Express. 2013; 21:2890–2902. [PubMed: 23481747]

60. Liang J, Williams DR, Miller DT. Supernormal vision and high-resolution retinal imaging through adaptive optics. J. Opt. Soc. Am. A. 1997; 14:2884–2892.
61. Neil MA, et al. Adaptive aberration correction in a two-photon microscope. J. Microsc. 2000; 200:105–108. [PubMed: 11106950]
62. Albert O, Sherman L, Mourou G, Norris TB, Vdovin G. Smart microscope: an adaptive optics learning system for aberration correction in multiphoton confocal microscopy. Opt. Lett. 2000; 25:52–54. [PubMed: 18059779]
63. Booth MJ, Neil MAA, Juškaitis R, Wilson T. Adaptive aberration correction in a confocal microscope. Proc. Natl Acad. Sci. USA. 2002; 99:5788–5792. [PubMed: 11959908]
64. Booth MJ. Adaptive optical microscopy: the ongoing quest for a perfect image. Light Sci. Appl. 2014; 3:e165.
65. Ji N, Milkie DE, Betzig E. Adaptive optics via pupil segmentation for high-resolution imaging in biological tissues. Nature Methods. 2010; 7:141–147. [PubMed: 20037592]
66. Cizmar T, Mazilu M, Dholakia K. In situ wavefront correction and its application to micromanipulation. Nature Photon. 2010; 4:388–394.
67. Kong L, Cui M. In vivo fluorescence microscopy via iterative multi-photon adaptive compensation technique. Opt. Express. 2014; 22:23786–23794. [PubMed: 25321957]
68. Fried DL. Anisoplanatism in adaptive optics. J. Opt. Soc. Am. 1982; 72:52–61.
69. Meng C, McDowell EJ, Yang C. An in vivo study of turbidity suppression by optical phase conjugation (TSOPC) on rabbit ear. Opt. Express. 2010; 18:25–30. [PubMed: 20173817]
70. Jang M, et al. Relation between speckle decorrelation and optical phase conjugation (OPC)-based turbidity suppression through dynamic scattering media: a study on in vivo mouse skin. Biomed. Opt. Express. 2015; 6:72–85. [PubMed: 25657876]
71. Leith EN, Upatnieks J. Holographic imagery through diffusing media. J. Opt. Soc. Am. 1966; 56:523–523.
72. Goodman JW, Huntley WH, Jackson DW, Lehmann M. Wavefront-reconstruction imaging through random media. Appl. Phys. Lett. 1966; 8:311–313.
73. Yariv A. Phase conjugate optics and real-time holography. IEEE J. Quantum Electron. 1978; 14:650–660.
74. Giuliano CR. Applications of optical phase conjugation. Phys. Today. 1981; 34(4):27–35.
75. Pepper DM. Nonlinear optical phase conjugation. Opt. Eng. 1982; 21:212156.
76. Fisher, RA. Optical Phase Conjugation. Academic; 1983.
77. Cui M, Yang C. Implementation of a digital optical phase conjugation system and its application to study the robustness of turbidity suppression by phase conjugation. Opt. Express. 2010; 18:3444–3455. [PubMed: 20389354]
78. Bellanger C, Brignon A, Colineau J, Huignard JP. Coherent fiber combining by digital holography. Opt. Lett. 2008; 33:2937–2939. [PubMed: 19079498]
79. Jang M, Ruan H, Zhou H, Judkewitz B, Yang C. Method for auto-alignment of digital optical phase conjugation systems based on digital propagation. Opt. Express. 2014; 22:14054–14071. [PubMed: 24977504]
80. Diaz Santana Haro L, Dainty JC. Single-pass measurements of the wave-front aberrations of the human eye by use of retinal lipofuscin autofluorescence. Opt. Lett. 1999; 24:61–63. [PubMed: 18071408]
81. Azucena O, et al. Wavefront aberration measurements and corrections through thick tissue using fluorescent microsphere reference beacons. Opt. Express. 2010; 18:17521–17532. [PubMed: 20721137]
82. Tao X, et al. Adaptive optics microscopy with direct wavefront sensing using fluorescent protein guide stars. Opt. Lett. 2011; 36:3389–3391. [PubMed: 21886220]
83. Wang K, et al. Rapid adaptive optical recovery of optimal resolution over large volumes. Nature Methods. 2014; 11:625–628. [PubMed: 24727653]
84. Rueckel M, Mack-Bucher JA, Denk W. Adaptive wavefront correction in two-photon microscopy using coherence-gated wavefront sensing. Proc. Natl Acad. Sci. USA. 2006; 103:17137–17142. [PubMed: 17088565]

85. Hermann B, et al. Adaptive-optics ultrahigh-resolution optical coherence tomography. Opt. Lett. 2004; 29:2142–2144. [PubMed: 15460883]
86. Lev A, Sfez B. In vivo demonstration of the ultrasound-modulated light technique. J. Opt. Soc. Am. A. 2003; 20:2347–2354.
87. Jang M, Ruan H, Judkewitz B, Yang C. Model for estimating the penetration depth limit of the time-reversed ultrasonically encoded optical focusing technique. Opt. Express. 2014; 22:5787–5807. [PubMed: 24663917]
88. Si K, Fiolka R, Cui M. Breaking the spatial resolution barrier via iterative sound-light interaction in deep tissue microscopy. Sci. Rep. 2012; 2:748. [PubMed: 23087813]
89. Suzuki Y, Tay JW, Yang Q, Wang LV. Continuous scanning of a time-reversed ultrasonically encoded optical focus by reflection-mode digital phase conjugation. Opt. Lett. 2014; 39:3441–3444. [PubMed: 24978506]
90. Ruan H, Jang M, Judkewitz B, Yang C. Iterative time-reversed ultrasonically encoded light focusing in backscattering mode. Sci. Rep. 2014; 4:7156. [PubMed: 25412687]
91. Judkewitz B, Wang YM, Horstmeyer R, Mathy A, Yang C. Speckle-scale focusing in the diffusive regime with time reversal of variance-encoded light (TROVE). Nature Photon. 2013; 7:300–305.
92. Liu Y, et al. Optical focusing deep inside dynamic scattering media with near-infrared time-reversed ultrasonically encoded (TRUE) light. Nature Commun. 2015; 6:5904. [PubMed: 25556918]
93. Newman JA, Webb KJ. Imaging optical fields through heavily scattering media. Phys. Rev. Lett. 2014; 113:263903. [PubMed: 25615337]
94. Laforest, T., et al. A 4000 Hz CMOS image sensor with in-pixel processing for light measurement and modulation; New Circuits and Systems Conf. (NEWCAS), IEEE 11th Intl; 2013. p. 1-4.
95. Vellekoop IM, Aegerter CM. Focusing light through living tissue. Proc. SPIE. 2010; 7554:755430.
96. Stockbridge C, et al. Focusing through dynamic scattering media. Opt. Express. 2012; 20:15086–15092. [PubMed: 22772205]
97. Nixon M, et al. Real-time wavefront shaping through scattering media by all-optical feedback. Nature Photon. 2013; 7:919–924.
98. Hollmann JL, Horstmeyer R, Yang C, DiMarzio CA. Diffusion model for ultrasound-modulated light. J. Biomed. Opt. 2014; 19:035005.
99. Dremeau A, et al. Reference-less measurement of the transmission matrix of a highly scattering material using a DMD and phase retrieval techniques. Opt. Express. 2015; 23:11898–11911. [PubMed: 25969280]
100. Yilmaz H, Vos WL, Mosk AP. Optimal control of light propagation through multiple-scattering media in the presence of noise. Biomed. Opt. Express. 2013; 4:1759–1768. [PubMed: 24049696]
101. van Beijnum F, van Putten EG, Lagendijk A, Mosk AP. Frequency bandwidth of light focused through turbid media. Opt. Lett. 2011; 36:373–375. [PubMed: 21283194]
102. Kohlgraf-Owens TW, Dogariu A. Transmission matrices of random media: means for spectral polarimetric measurements. Opt. Lett. 2010; 35:2236–2238. [PubMed: 20596205]
103. Fink M. Time reversed acoustics. Phys. Today. 1997; 50(3):34–40.
104. Lerosey G, de Rosny J, Tourin A, Fink M. Focusing beyond the diffraction limit with far-field time reversal. Science. 2007; 315:1120–1122. [PubMed: 17322059]
105. Aulbach J, Gjonaj B, Johnson PM, Mosk AP, Lagendijk A. Control of light transmission through opaque scattering media in space and time. Phys. Rev. Lett. 2011; 106:103901. [PubMed: 21469791]
106. McCabe DJ, et al. Spatio-temporal focusing of an ultrafast pulse through a multiply scattering medium. Nature Commun. 2011; 2:447. [PubMed: 21863014]
107. Katz O, Small E, Bromberg Y, Silberberg Y. Focusing and compression of ultrashort pulses through scattering media. Nature Photon. 2011; 5:372–377.
108. Paudel HP, Stockbridge C, Mertz J, Bifano T. Focusing polychromatic light through strongly scattering media. Opt. Express. 2013; 21:17299–17308. [PubMed: 23938576]
109. Vogel A, Venugopalan V. Mechanisms of pulsed laser ablation of biological tissues. Chem. Rev. 2003; 103:577–644. [PubMed: 12580643]

110. Goto K, Nakagawa T, Nakamura O, Kawata S. An implantable power supply with an optically rechargeable lithium battery. IEEE Trans. Biomed. Eng. 2001; 48:830–833. [PubMed: 11442295]

111. Williams JC, Denison T. From optogenetic technologies to neuromodulation therapies. Sci. Transl. Med. 2013; 5:177ps6.

112. Yoon J, et al. Optogenetic signaling-pathway regulation through scattering skull using wavefront shaping. 2015 Preprint at http://arxiv.org/abs/1502.04826.

113. Papagiakoumou E, et al. Functional patterned multiphoton excitation deep inside scattering tissue. Nature Photon. 2013; 7:274–278.

114. van Putten EG, Lagendijk A, Mosk AP. Optimal concentration of light in turbid materials. J. Opt. Soc. Am. B. 2011; 28:1200–1203.

115. Volpe G, Kurz L, Callegari A, Volpe G, Gigan S. Speckle optical tweezers: micromanipulation with random light fields. Opt. Express. 2014; 22:18159–18167. [PubMed: 25089434]

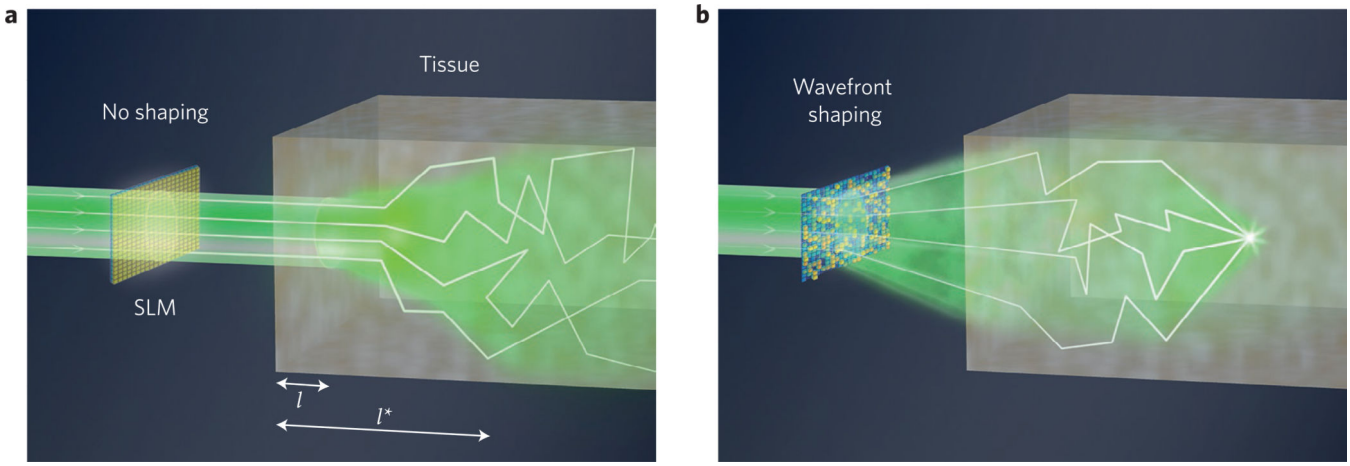

Figure 1. Principle of wavefront shaping

a, An unmodified coherent beam of light travels one mean free path (*l*) with minimal scattering into tissue. A fraction of beam directionality is preserved up to the transport mean free path length, *l**. **b**, By wavefront-shaping the incident field with an SLM, it is possible to focus within tissue beyond *l**.

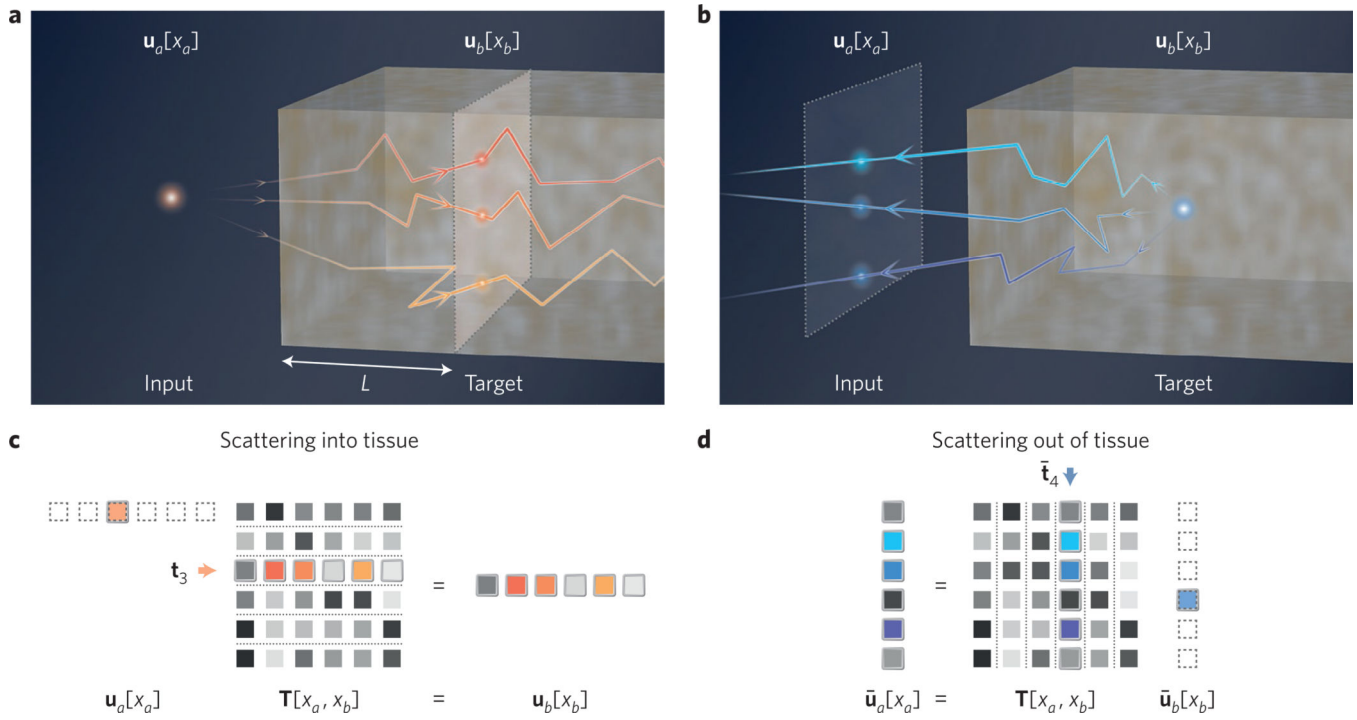

Figure 2. Matrix model of scattering in tissue

a, Forward optical scattering into tissue (distance L, input to target plane). **b**, Reverse optical scattering out of tissue (target to input plane). **c**, Transmission matrix model for forward scattering. A discrete input point source at position 3 sets $\mathbf{u}_a[x_a] = \delta_3$, the third unit vector. The target field is then $\mathbf{t}_3$, the third transmission matrix row. **d**, Matrix model for scattering from an embedded guidestar point, which sets $\bar{\mathbf{u}}_b[x_b] = \bar{\delta}_4$ (column vector). Assuming time-reversal symmetry, the input plane field becomes $\bar{\mathbf{t}}_4$, the fourth transmission matrix column.

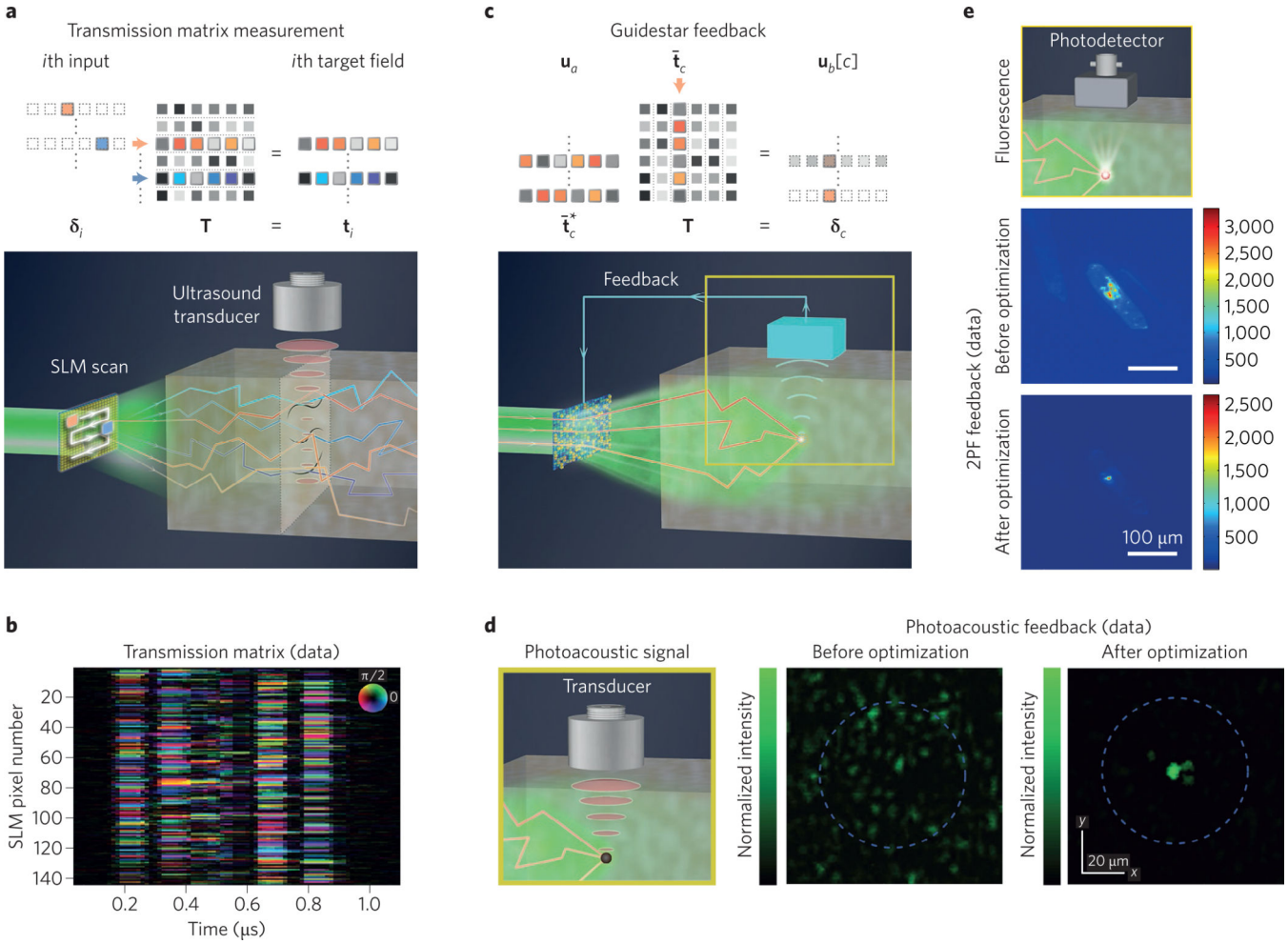

Figure 3. Feedback guidestars

a, Measuring the optical transmission matrix. Rows of **T** are sampled by scanning one transparent pixel across an input SLM and detecting each target field. From within tissue, an external transducer obtains indirect measurements via the photo-acoustic effect. **b**, Compiled together, these photo-acoustic measurements form an optical transmission matrix[17]. **c**, Feedback guidestar matrix model, with measurements from one discrete location within tissue, $\mathbf{u}_b[3]$. **d**, Photo-acoustic feedback measured via an ultrasound transducer optimizes light delivery to a tight focus[20]. **e**, Fluorescence feedback, such as two-photon fluorescence (2PF). After optimization, 2PF feedback focuses light through $L = 1$ mm of brain tissue[56]. Figure reproduced with permission from: **e**, ref. 56, OSA.

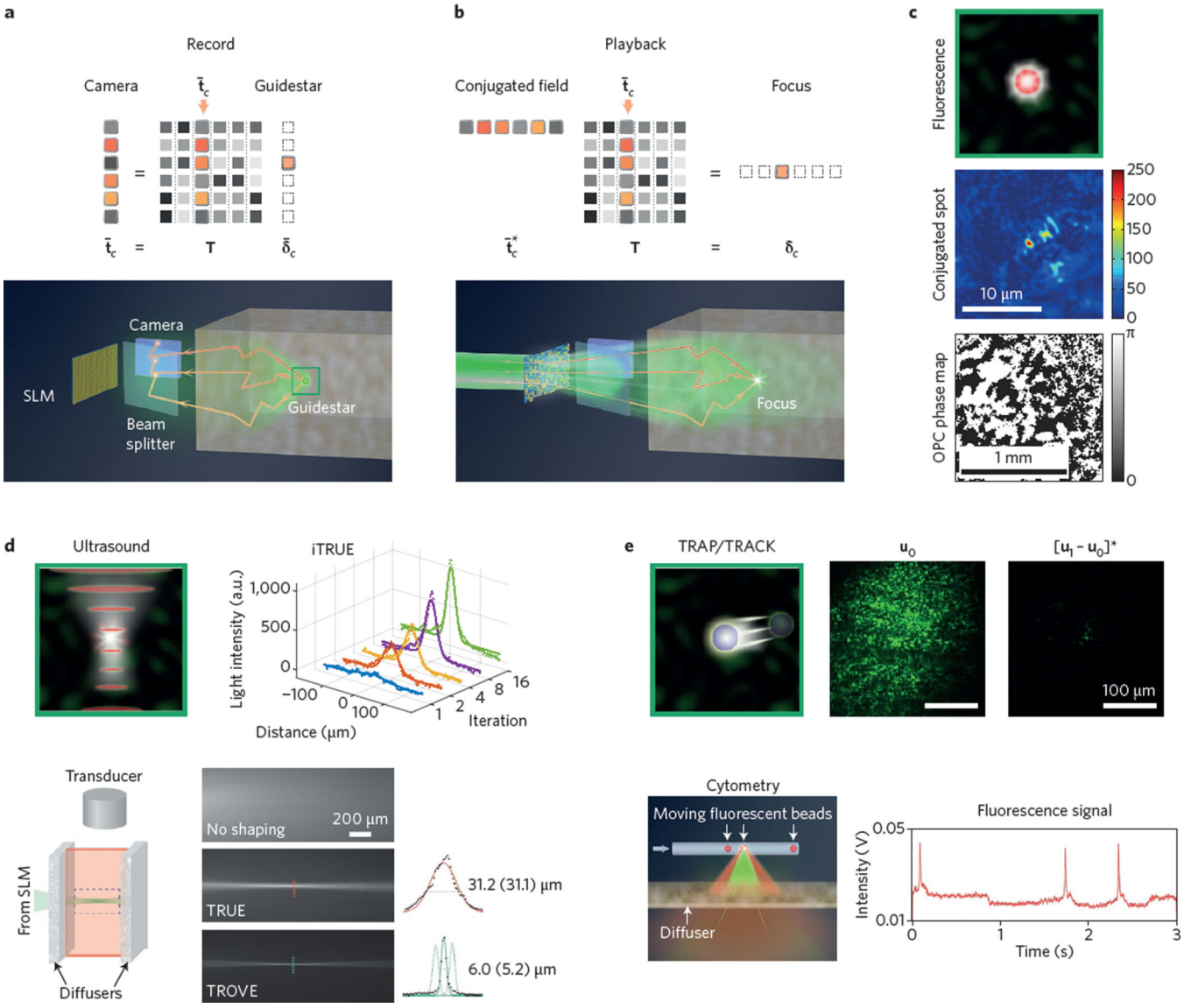

Figure 4. Conjugation guidestars

a, Matrix model and set-up for detecting an embedded guidestar field. Light from target field spot δ_3 forms the speckle field $\mathbf{t}_3$ at the input plane camera. **b**, Matrix model and set-up for conjugation guidestar focusing. SLM-shaping an incident wavefront into conjugate field $\mathbf{t}_3^*$ refocuses to δ_3. **c**, Fluorescent conjugation guidestar experiment (0.2 µm bead), with resulting focus and conjugate phase map[15]. **d**, Ultrasound conjugation guidestar experiments. iTRUE sharpens the conjugated spot size[90] by a factor of three. TROVE reduces the focal spot width[91] from 31 µm to 5 µm. **e**, Kinematic target conjugation guidestar experiments (TRAP/TRACK). The resulting focus enables particle counting[25]. Figure reproduced with permission from: **c**, ref. [15], AIP; **e**, ref. 25, OSA.

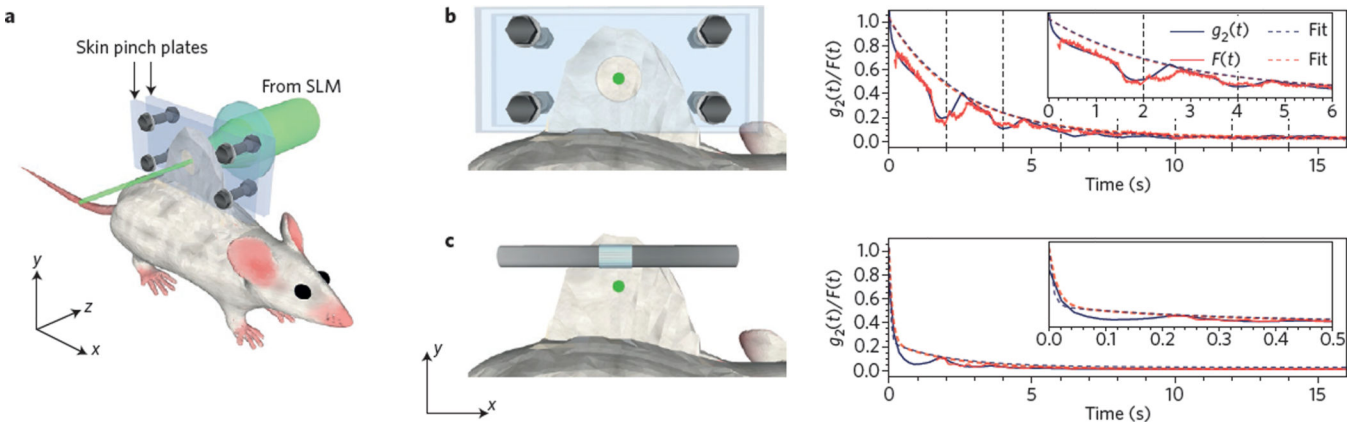

Figure 5. Tissue motion dims an OPC focus

a, Diagram of OPC decorrelation experiment, where wavefront shaping forms a tight focus through pinched, *in vivo* mouse tissue. **b**, Focusing light through partially immobilized dorsal skin. Both the speckle autocorrelation ($g_2(t)$, black) and OPC focal spot intensity ($F(t)$, red) decay in magnitude over the course of several seconds, with fitted curves. **c**, In unconstrained skin, decorrelation occurs on a much faster (sub-second) timescale. Figure reproduced with permission from ref. 70, OSA.

Table 1

List of biological tissue guidestars for feedback and conjugation.

Guidestar mechanism		Ref.	Minimum spot size	Non-invasive?	Translate position?	PBR	Required time (s)	Coupling efficiency
Conjugation guidestar	Fluorescence	14, 53, 114	1 μm	No	No	20–40	10^3	Low
	Ultrasound	55	1 mm	Yes	Yes	10	10^3–10^4	Low
	Photo-acoustic	18, 19	35 μm	Yes	Yes	5–10	10^3	Moderate
	Nonlinear photo-acoustic	20	5 μm	Yes	Yes	6,000	10^3	Moderate
	Two-photon	56, 57	1–5 μm	Yes *	Yes	20	10^3–10^4	Moderate
	Coherence gating	58, 59	1 μm	Yes	Yes	50	1–10	Moderate
Feedback guidestar	Second harmonic	16	2 μm	No	No	400	1	Moderate
	Fluorescence	15	1 μm	No	No	10–100	10^2	Moderate
	Ultrasound	21_23	30 μm	Yes	Yes	5	<1	Low
	Iterative ultrasound	88_90	10 μm	Yes	Yes	30	1–10	Low
	Variance-encoded ultrasound (TROVE)	91	5 μm	Yes	Yes	100	10^3–10^4	Low
	Particle displacement (TRAP, TRACK)	24, 25	5–10 μm	Yes *	Yes	300	<1	High

Minimum spot size selected as minimum across all similar demonstrations. Peak-to-background ratio (PBR) selected as maximum across all similar demonstrations. Required time is an order of magnitude approximation. Coupling efficiency p, defined as the percentage of incident optical power transferred into a detectable guidestar signal, is high if $p > 0.5$, moderate if $0.5 > p > 0.01$, and low if $p < 0.01$.

* Possible invasive insertion used in experiment, but not required in principle.